Coherent diffractive imaging beyond the projection approximation: waveguiding at extreme ultraviolet wavelengths

Sergey Zayko,[1] **Eike Mönnich,**[1] **Murat Sivis,**[1] **Dong-Du Mai,**[2] **Tim Saldit,**[2] **Sascha Schäfer,**[1] **and Claus Ropers**[1,*]

[1]*IV. Physical Institute - Solids and Nanostructures, University of Göttingen, 37077 Göttingen, Germany*
[2]*Institute for X-Ray Physics, University of Göttingen, 37077 Göttingen, Germany*

[*]*cropers@gwdg.de*

Abstract: We study extreme-ultraviolet wave propagation within optically thick nanostructures by means of high-resolution coherent diffractive imaging using high-harmonic radiation. Exit waves from different objects are reconstructed by phase retrieval algorithms, and are shown to be dominated by waveguiding within the sample. The experiments provide a direct visualization of extreme-ultraviolet guided modes, and demonstrate that multiple scattering is a generic feature in extruded nanoscale geometries. The observations are successfully reproduced in numerical and semi-analytical simulations.

References and links

1. M. Born and E. Wolf, *Principles of Optics: Electromagnetic Theory of Propagation, Interference and Diffraction of Light* (Cambridge University, 1999).
2. P. Thibault, M. Dierolf, A. Menzel, O. Bunk, C. David, and F. Pfeiffer, "High-resolution scanning x-ray diffraction microscopy," Science **321**, 379–382 (2008).
3. H. F. Schouten, N. Kuzmin, G. Dubois, T. D. Visser, G. Gbur, P. F. A. Alkemade, H. Blok, G. W. t. Hooft, D. Lenstra, and E. R. Eliel, "Plasmon-assisted two-slit transmission: Young's experiment revisited," Phys. Rev. Lett. **94**, 053901 (2005).
4. C. Mack, *Fundamental Principles of Optical Lithography: The Science of Microfabrication* (Wiley, 2007).
5. A. Poonawala and P. Milanfar, "Mask design for optical microlithography mdash;an inverse imaging problem," IEEE Trans. Image Processing **16**, 774–788 (2007).
6. K. A. Goldberg, E. Tejnil, and J. Bokor, "A 3-d numerical study of pinhole diffraction to predict the accuracy of EUV point diffraction interferometry," Tech. rep., Lawrence Berkeley National Lab., CA (United States) (1995).
7. A. Hare and G. Morrison, "Near-field soft x-ray diffraction modelled by the multislice method," J. Mod. Opt. **41**, 31–48 (1994).
8. A. I. Erko, M. Idir, T. Krist, and A. G. Michette, *Modern Developments in X-ray and Neutron Optics*, vol. 137 (Springer, 2008).
9. J. Miao, P. Charalambous, J. Kirz, and D. Sayre, "Extending the methodology of x-ray crystallography to allow imaging of micrometre-sized non-crystalline specimens," Nature **400**, 342–344 (1999).
10. H. N. Chapman, A. Barty, M. J. Bogan, S. Boutet, M. Frank, S. P. Hau-Riege, S. Marchesini, B. W. Woods, S. Bajt, W. H. Benner, R. A. London, E. Plonjes, M. Kuhlmann, R. Treusch, S. Dusterer, T. Tschentscher, J. R. Schneider, E. Spiller, T. Moller, C. Bostedt, M. Hoener, D. A. Shapiro, K. O. Hodgson, D. van der Spoel,

F. Burmeister, M. Bergh, C. Caleman, G. Huldt, M. M. Seibert, F. R. N. C. Maia, R. W. Lee, A. Szoke, N. Tim-neanu, and J. Hajdu, "Femtosecond diffractive imaging with a soft-x-ray free-electron laser," Nat. Phys **2**, 839–843 (2006).

11. R. L. Sandberg, A. Paul, D. A. Raymondson, S. Hädrich, D. M. Gaudiosi, J. Holtsnider, R. I. Tobey, O. Cohen, M. M. Murnane, H. C. Kapteyn, C. Song, J. Miao, Y. Liu, and F. Salmassi, "Lensless diffractive imaging using tabletop coherent high-harmonic soft-x-ray beams," Phys. Rev. Lett. **99**, 098103 (2007).

12. M. D. Seaberg, D. E. Adams, E. L. Townsend, D. A. Raymondson, W. F. Schlotter, Y. Liu, C. S. Menoni, L. Rong, C. C. Chen, J. Miao, H. C. Kapteyn, and M. M. Murnane, "Ultrahigh 22 nm resolution coherent diffractive imaging using a desktop 13 nm high harmonic source," Opt. Express **19**, 22470–22479 (2011).

13. B. Zhang, M. D. Seaberg, D. E. Adams, D. F. Gardner, E. R. Shanblatt, J. M. Shaw, W. Chao, E. M. Gullikson, F. Salmassi, H. C. Kapteyn, and M. M. Murnane, "Full field tabletop EUV coherent diffractive imaging in a transmission geometry," Opt. Express **21**, 21970–21980 (2013).

14. A. Ravasio, D. Gauthier, F. R. N. C. Maia, M. Billon, J. Caumes, D. Garzella, M. Géléoc, O. Gobert, J.-F. Hergott, A.-M. Pena, H. Perez, B. Carré, E. Bourhis, J. Gierak, A. Madouri, D. Mailly, B. Schiedt, M. Fajardo, J. Gautier, P. Zeitoun, P. H. Bucksbaum, J. Hajdu, and H. Merdji, "Single-shot diffractive imaging with a table-top femtosecond soft x-ray laser-harmonics source," Phys. Rev. Lett. **103**, 028104 (2009).

15. S. Flewett, S. Schaffert, J. Mohanty, E. Guehrs, J. Geilhufe, C. M. Günther, B. Pfau, and S. Eisebitt, "Method for single-shot coherent diffractive imaging of magnetic domains," Phys. Rev. Lett. **108**, 223902 (2012).

16. M. Zürch, J. Rothhardt, S. Hadrich, S. Demmler, M. Krebs, J. Limpert, A. Tunnermann, A. Guggenmos, U. Kleineberg, and C. Spielmann, "Real-time and sub-wavelength ultrafast coherent diffraction imaging in the extreme ultraviolet," Sci. Rep. **4**, 7356 (2014).

17. S. Eisebitt, J. Lüning, W. Schlotter, M. Lörgen, O. Hellwig, W. Eberhardt, and J. Stöhr, "Lensless imaging of magnetic nanostructures by x-ray spectro-holography," Nature **432**, 885–888 (2004).

18. M. A. Pfeifer, G. J. Williams, I. A. Vartanyants, R. Harder, and I. K. Robinson, "Three-dimensional mapping of a deformation field inside a nanocrystal," Nature **442**, 63–66 (2006).

19. A. McPherson, G. Gibson, H. Jara, U. Johann, T. S. Luk, I. A. McIntyre, K. Boyer, and C. K. Rhodes, "Studies of multiphoton production of vacuum-ultraviolet radiation in the rare gases," J. Opt. Soc. Am. B **4**, 595–601 (1987).

20. X. F. Li, A. L'Huillier, M. Ferray, L. A. Lompré, and G. Mainfray, "Multiple-harmonic generation in rare gases at high laser intensity," Phys. Rev. A **39**, 5751–5761 (1989).

21. C. Winterfeldt, C. Spielmann, and G. Gerber, "Colloquium: Optimal control of high-harmonic generation," Rev. Mod. Phys. **80**, 117–140 (2008).

22. J. Spence, U. Weierstall, and M. Howells, "Coherence and sampling requirements for diffractive imaging," Ultramicroscopy **101**, 149–152 (2004).

23. B. Chen, B. Abbey, R. Dilanian, E. Balaur, G. van Riessen, M. Junker, C. Q. Tran, M. W. M. Jones, A. G. Peele, I. McNulty, D. J. Vine, C. T. Putkunz, H. M. Quiney, and K. A. Nugent, "Diffraction imaging: The limits of partial coherence," Phys. Rev. B **86**, 235401 (2012).

24. J. Miao, T. Ishikawa, E. H. Anderson, and K. O. Hodgson, "Phase retrieval of diffraction patterns from noncrystalline samples using the oversampling method," Phys. Rev. B **67**, 174104 (2003).

25. J. R. Fienup, "Phase retrieval algorithms: a comparison," Appl. Opt. **21**, 2758–2769 (1982).

26. S. Marchesini, "Invited article: a [corrected] unified evaluation of iterative projection algorithms for phase retrieval." Rev. Sci. Instrum. **78**, 011301 (2007).

27. D. R. Luke, "Relaxed averaged alternating reflections for diffraction imaging," Inverse Problems **21**, 37 (2005).

28. D. Shapiro, P. Thibault, T. Beetz, V. Elser, M. Howells, C. Jacobsen, J. Kirz, E. Lima, H. Miao, A. M. Neiman, and D. Sayre, "Biological imaging by soft x-ray diffraction microscopy," Proc. Nat. Acad. Sci. USA **102**, 15343–15346 (2005).

29. H. N. Chapman, A. Barty, S. Marchesini, A. Noy, S. P. Hau-Riege, C. Cui, M. R. Howells, R. Rosen, H. He, J. C. H. Spence, U. Weierstall, T. Beetz, C. Jacobsen, and D. Shapiro, "High-resolution ab initio three-dimensional x-ray diffraction microscopy," J. Opt. Soc. Am. A **23**, 1179–1200 (2006).

30. Note that a weak stripe-like contrast in the depth of the structure does not correspond to a step, but arises from chemical contrast from a 4 nm thick Titanium adhesion layer between the silicon nitride (Si_3N_4) and gold layers.

31. COMSOL Multiphysics, Wave Optics Module.

32. C. Fuhse and T. Salditt, "Finite-difference field calculations for two-dimensionally confined x-ray waveguides," Appl. Opt. **45**, 4603–4608 (2006).

33. C. Fuhse and T. Salditt, "Propagation of x-rays in ultra-narrow slits," Optics Communications **265**, 140 – 146 (2006).

34. Atomic Data and Nuclear Data Tables Vol. 54 (no.2), 181-342 (1993).

35. C. L. Chen, *Foundations for Guided-Wave Optics* (John Wiley & Sons, 2006).

36. K. S. Raines, S. Salha, R. L. Sandberg, H. Jiang, J. A. Rodriguez, B. P. Fahimian, H. C. Kapteyn, J. Du, and J. Miao, "Three-dimensional structure determination from a single view," Nature **463**, 214–217 (2010).

37. A. V. Martin, F. Wang, N. D. Loh, T. Ekeberg, F. R. N. C. Maia, M. Hantke, G. van der Schot, C. Y. Hampton, R. G. Sierra, A. Aquila, S. Bajt, M. Barthelmess, C. Bostedt, J. D. Bozek, N. Coppola, S. W. Epp, B. Erk, H. Fleckenstein, L. Foucar, M. Frank, H. Graafsma, L. Gumprecht, A. Hartmann, R. Hartmann, G. Hauser,

H. Hirsemann, P. Holl, S. Kassemeyer, N. Kimmel, M. Liang, L. Lomb, S. Marchesini, K. Nass, E. Pedersoli, C. Reich, D. Rolles, B. Rudek, A. Rudenko, J. Schulz, R. L. Shoeman, H. Soltau, D. Starodub, J. Steinbrener, F. Stellato, L. Strüder, J. Ullrich, G. Weidenspointner, T. A. White, C. B. Wunderer, A. Barty, I. Schlichting, M. J. Bogan, and H. N. Chapman, "Noise-robust coherent diffractive imaging with a single diffraction pattern," Opt. Express **20**, 16650–16661 (2012).

38. K. Giewekemeyer, P. Thibault, S. Kalbfleisch, A. Beerlink, C. M. Kewish, M. Dierolf, F. Pfeiffer, and T. Salditt, "Quantitative biological imaging by ptychographic x-ray diffraction microscopy." Proc. Nat. Acad. Sci.U.S.A. **107**, 529–34 (2010).

39. S. Marchesini, H. He, H. N. Chapman, S. P. Hau-Riege, A. Noy, M. R. Howells, U. Weierstall, and J. C. H. Spence, "X-ray image reconstruction from a diffraction pattern alone," Phys. Rev. B **68**, 140101 (2003).

Classical diffraction theory, within the descriptions of Fresnel, Kirchhoff and Fraunhofer, considers field distributions initially given on a two-dimensional plane [1]. In the most common cases, including those for which closed solutions exist, the initial fields are represented by constant amplitudes on apertures of a compact support. Approximating such conditions experimentally usually involves the illumination of opaque screens with apertures by a collimated beam of light, with a prominent classroom demonstration being Young's double-slit experiment. A frequent implicit assumption is that the screen geometrically carves out the aperture shape from the incident beam profile, and that no diffraction occurs within the thickness, i.e., the longitudinal dimensions, of the screen. Mathematically speaking, the scattered light can be represented as a product of the illuminating field and the complex transmission function $\tau(x,y)$ of the aperture. For hard x-rays, in the commonly employed projection approximation, τ is derived by integrating the optical indices over the object thickness L. This is justified as long as, for the wavelength λ used, the Fresnel number $F = a^2/(\lambda \cdot L)$ for diffraction *inside* the object remains much larger than unity, where a is a typical transverse length in the object. A related condition on the validity of the factorization approach is given in Ref. [2].

In the case of three-dimensional geometries, wave propagation within the sample may drastically alter the diffraction by an object. For example, surface plasmon polariton contributions may significantly affect double-slit interference [3]. In the presence of optically dense media, multiply scattered waves may experience confinement and waveguiding in the exit wave formation. In particular, at extreme ultraviolet (EUV) wavelengths, such phenomena are technologically important in nanoscale mask design for lithography [4–8]. Coherent diffractive imaging (CDI) [9–16] provides immediate access to amplitude- and phase-resolved exit wave distributions, and attention has largely been paid to accurate object representation and spatial resolution, including a variety of contrast mechanisms such as magnetism [17] or strain [18]. However, CDI has not yet been used to directly visualize multiple scattering and wave confinement.

In this Letter, we utilize CDI with EUV high-harmonic radiation [19, 20] to elucidate wave propagation within tailored, optically thick nanostructures. We demonstrate pronounced waveguiding effects for various geometric parameters, indicating the universal relevance of three-dimensional diffraction phenomena in this spectral range and for typical mask dimensions and aspect ratios. Moreover, we find that for extreme-ultraviolet CDI, spatial mode filtering within thick objects poses a more severe constraint on the achievable spatial resolution than the fundamental limit given by the numerical aperture of detection. The experimental observations are in good agreement with results of numerical finite element modeling and a semi-analytical modal expansion.

CDI experiments are carried out in a high-vacuum setup as schematically depicted in Fig. 1. High-harmonic up-conversion of amplified laser pulses (450 μJ pulse energy, 40 fs pulse duration, 800 nm central-wavelength, 1 kHz repetition rate) is induced in an argon-filled capillary, leading to a broad spectrum of discrete harmonics [21]. Details of the generation conditions and EUV photon flux are provided in the Appendix. A 150 nm thick aluminum foil blocks the fundamental laser beam, transmitting the EUV light with minor losses. The 23rd harmonic or-
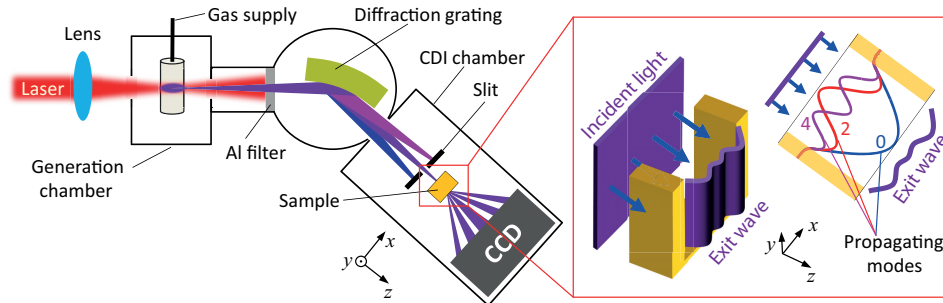
Fig. 1. Schematic of the experimental setup displaying the high-harmonic generation chamber, the diffraction grating and the imaging chamber (CDI chamber). The inset illustrates the modification of the exit wave induced by propagating waveguide modes within the extended structure (three even modes denoted by mode indices).

der (wavelength $\lambda = 34.8$ nm) in the plateau region of the HHG spectrum is spectrally selected and focused onto the sample by a blazed toroidal grating (550 grooves/mm) and a moveable slit close to the sample position. The use of the diffraction grating serves two purposes: (i) selecting an individual harmonic and separating it from the fundamental beam, and (ii) for objects smaller than a dispersed harmonic in the focal plane, the spatial dispersion of the grating provides for an illumination with enhanced monochromaticity. This allows for an increased number of resolution elements in imaging, i.e., a larger field of view for a given resolution [22, 23]. Coherent diffraction patterns from several non-periodic samples are recorded at distances of $L = 20$ mm (object A) and $L = 30$ mm (object B) by a cooled, back-illuminated charge-coupled device (CCD) camera (20 μm pixel size, 1340 x 1300 array), ensuring sufficient oversampling [24] and a high numerical aperture (NA). The samples are prepared by focused ion beam etching of gold films (460 nm (object A) and 150 nm (object B) thickness) on 200 nm silicon nitride membranes. Scanning electron micrographs (SEM) of objects A and B are shown in the insets of Fig. 2(b) and 2(e), respectively, with dark regions corresponding to aperture areas in the samples.

Figures 2(a), 2(d) show coherent diffraction patterns of objects A and B. The diffraction intensity and its coherent modulation extend to high numerical apertures, even beyond the detector area for some principal directions. Interestingly, the diffraction patterns are not centro-symmetric, which implies a non-trivial phase-structure of the exit wave. The images are recorded without blocking the intense central part (no beam stop), so that all spatial frequencies are contained in one acquisition, facilitating exit wave reconstructions (b,e: amplitudes; c,f: phases) by iterative phase retrieval algorithms [25, 26]. We successfully reconstruct the complex-valued exit wave using a variety of different algorithms, with best results obtained with the Relaxed Averaged Alternating Reflections (RAAR) algorithm [27]. A support constraint was generated from the objects autocorrelation function (calculated as the inverse Fourier transform of the diffraction pattern) [25]. We apply a phase retrieval transfer function [10, 28, 29] to estimate the resolution determined by the reconstruction algorithm. The phases are reliably retrieved up to the corners of the detector – above 15 μm^{-1}, indicating a diffraction limited resolution. Further experimental details concerning image acquisition, processing and reconstruction are given in the Appendix.

In general, the reconstructed amplitudes and phases represent the distribution of apertures in the otherwise opaque masks, in agreement with the SEM characterization. However, closer inspection reveals significant spatial amplitude and phase modulations, with pronounced dependencies on local aperture width. Fourier truncation artifacts can be ruled out as a cause for
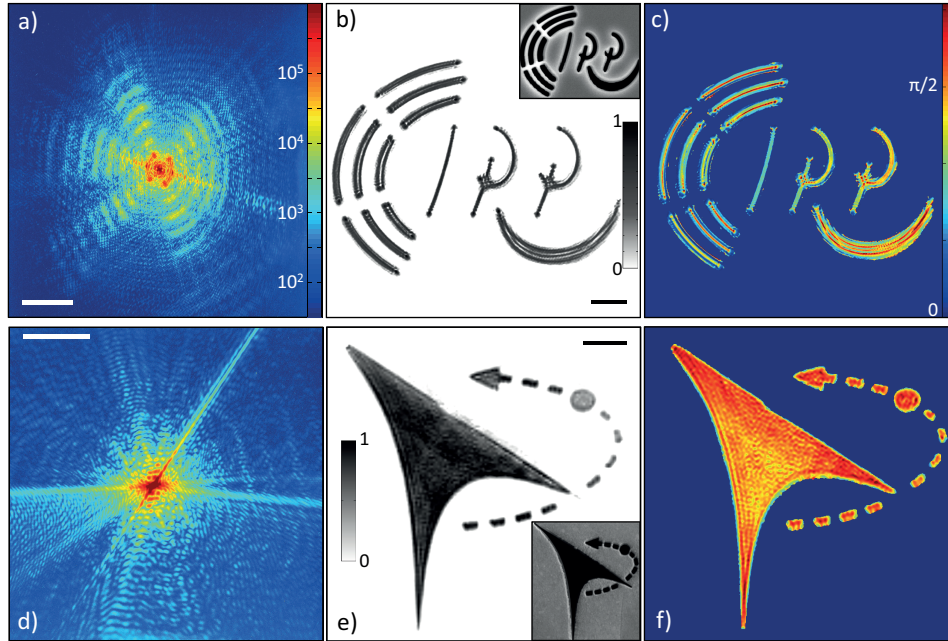
Fig. 2. (a) Coherent diffraction patterns (a), (d) on a logarithmic scale, reconstructed exit wave amplitudes (b), (e) in arb. units and phases (c), (f) in radians of objects A (top row) and B (bottom row). Insets in (b), (e) display scanning electron micrographs. Scale bars: 5 μm^{-1} (a), (d); 1 μm (b), (e). Identical colormaps are used for both objects in (a), (d) and (c), (f).

these features (see Appendix), and, as we show in the following, these field distributions can be directly attributed to waveguiding effects.

Figure 3 compares cross-sections through the reconstructed exit wave amplitude with simulated field distributions in planar waveguides of corresponding dimensions. Three selected positions for lineouts are indicated in a tilted-view SEM image of object A (Fig. 3(a)) and the reconstructed field amplitude (Fig. 3(b)) [30]. The cross-sectional shapes of the marked features in the reconstruction vary from a single lobe at line L1 to two and three maxima at lines L2 and L3, respectively. The structure widths at these positions are on the order of 150 (L1), 400 (L2) and 500 nm (L3), estimated from backside SEM images (see Appendix). With a depth L close to 700 nm, diffraction within the structure is characterized by Fresnel numbers of 0.6, 5.9 and 9.5 respectively. Roughly corresponding to slit-type geometries, these parts of the sample induce an effectively one-dimensional confinement for the incident light at a wavelength of 34.8 nm. For the dimensions given, we carry out numerical simulations of the wave propagation within the structure using finite element modeling [31].

Figure 3(c) displays the results of two-dimensional simulations of the electric field propagation along waveguides of different thicknesses corresponding to the positions given in Figs. 3(a) and 3(b). In the simulations, the incident polarization was chosen to approximate the experimental conditions, i.e., perpendicular to the waveguide slab at positions 1 and 2 (leading to transverse magnetic (TM) modes) and parallel to the slab at position 3 (leading to transverse electric (TE) modes). With the refractive indices of the cladding materials incorporated in the simulations, the computed exit wave amplitudes (Fig. 3(c), red dotted lines) closely follows the experimental lineouts (Fig. 3(c), blue solid). For simplicity, the small tapering of the
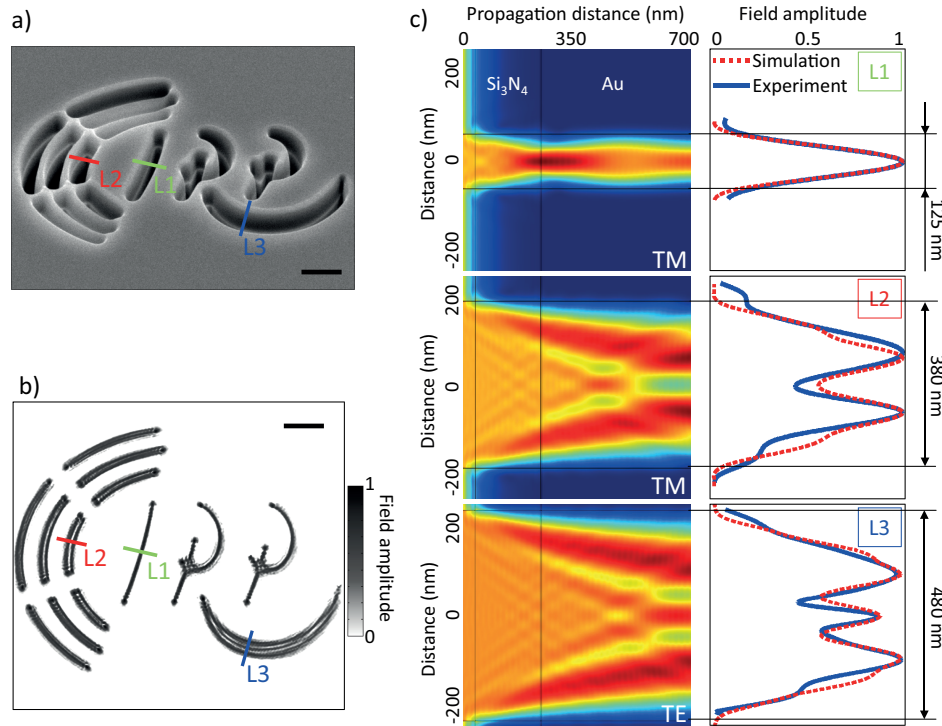
Fig. 3. (a) Tilted view SEM image of object A. (b) Magnitude of the reconstructed exit field, indicating positions of cross-sections chosen for comparison with wave-guide simulations. (c) Finite element simulations of the wave propagation in slab waveguides of dimensions and materials corresponding to experimental conditions (see text). Left column: Evolution of field magnitudes along the propagation direction for three waveguide widths chosen according to the respective lineouts in (a) and (b). Right column: Comparison of simulated exit field magnitudes (dotted red) with experimental profiles (solid blue). Scale bars are 1 μm.

waveguides following fabrication (estimated as below 5 degrees half taper angle from SEM characterization) was not included in the simulations, as it is not expected to induce substantial qualitative changes. We obtain very similar results with finite-difference field calculations based on a parabolic wave equation [32, 33] and a semi-analytical solution of the waveguide propagation using a modal expansion (see Appendix).

In addition, the modal expansion provides further insight into the waveguiding characteristics in the EUV, where high propagation losses are expected for most cladding materials, e.g. refractive index of gold at 34.8 nm: n = 0.77+0.39i [34]. Figure 4 displays real and imaginary parts of the propagation constants β_n, i.e. the wavenumber of mode n, for the lowest order TM and TE modes in a gold-cladded vacuum waveguide as a function of waveguide widths, computed by numerically solving the well-known characteristic equations [35]. Only modes with even indices are shown, since these are the ones excited by far-field radiation under normal incidence. The inset shows the corresponding mode transmission for a waveguide length of 700 nm. In agreement with the simulations in Fig. 3, it is apparent that for the smaller features around 100 nm width, the fundamental mode presents the dominant contribution with a minor additional component from a second even mode. For larger widths, several modes interfere with almost equal amplitude, and the beating of these modes along the waveguide depth
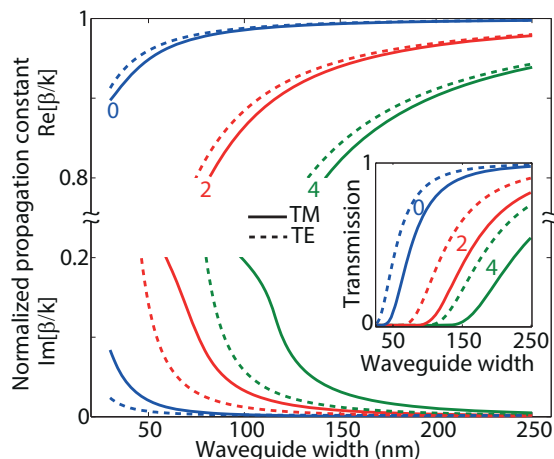
Fig. 4. Real (top curves) and imaginary (bottom curves) parts of the propagation constant for the first three even TM (solid) and TE (dotted) modes, normalized to the vacuum wave number. Inset: Transmission coefficients through a 700 nm long gold waveguide of different widths.

determines the exit wave intensity distribution. It is important to note that, due to the enhanced losses of higher order modes, the channels act as effective low-pass filters suppressing high-angle scattering. Therefore, as demonstrated here, the achievable resolution in the imaging of extruded structures may often be limited by waveguiding instead of the numerical aperture of the detection system.

Generally, because of the higher surface reflectivity for light polarization parallel to the waveguide cladding, TE modes exhibit somewhat lower damping and higher transmission. This effect may be used for polarization filtering of the transmitted light. To give a numerical example, in a tradeoff between polarization contrast and TE transmission, polarization contrasts of 10^2 and 10^3 may be obtained at mode transmissions of 15 % and 6 %, respectively, for a 300 nm long waveguide.

In conclusion, we have presented lensless imaging experiments with a table-top high-harmonic source, reconstructing the exit waves of different non-periodic samples. Strong spatial modulations of the field distributions are caused by multiple scattering within the sample, and theoretical modeling accurately reproduces the experimental findings. Besides applications in nanoscale lithography, the phase-resolved imaging of guided modes enables further investigations of waveguiding properties in the EUV spectral range, and is expected to result in the development of new optical devices, such as polarizers, mode filters or wave plates for EUV and soft X-ray radiation.

Appendix A: sample details

The samples are prepared by focused ion beam (FIB) etching of 200 nm thick silicon nitride membranes coated with a layer of gold (thicknesses of 460 nm and 150 nm for object A and B, respectively) on a titanium adhesion layer (4 nm thickness). In addition, a 40 nm thick titanium layer is deposited on the opposite side of sample A. The ion beam focusing and current conditions were iteratively optimized to obtain small taper angles in the structures. In the experiment, the samples are illuminated from different sides, as illustrated in Fig. 5(a). Sample characterization was carried out by scanning electron microscopy. Exemplary image from the back side of object A is shown in Fig. 5(b).
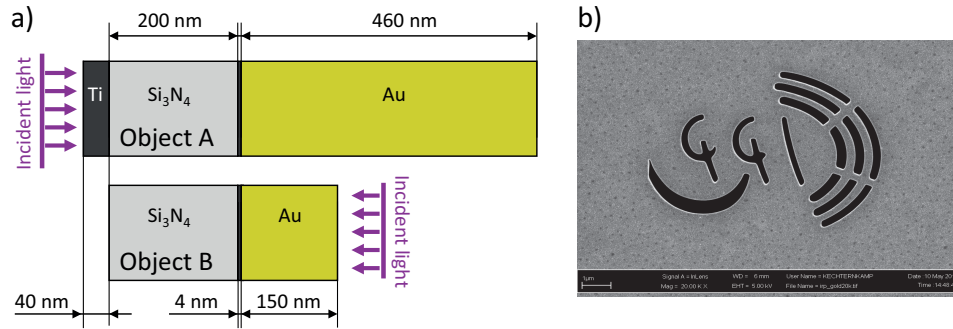
Fig. 5. (a) Schematic of the layered structure of object A (top) and B (bottom). (b) Scanning electron micrograph of object A, recorded from the back side (gold). Focused ion beam milling was carried out from the front side. Note that the apparent width of the waveguides depends on the SEM focus settings, which gives rise to an uncertainty in the measured widths of several tens of nanometers.

Appendix B: high-harmonic generation

For improved conversion efficiency of the generation process, phase-matching is optimized by tuning the gas pressure inside the capillary and the laser focusing conditions. Specifically, the highest yield of the 23rd harmonic order (34.8 nm) is obtained at a pressure of 75 mbar and by focusing the laser at the end of the 8 mm long capillary (focal length 20 cm). The measured photon flux (incident on the sample) of the 23rd harmonic order is $3.4 \cdot 10^5$ photons/pulse. The detector was intensity calibrated at the BESSY II, PTB Laboratory.

Appendix C: reconstruction

The diffraction pattern of object A (Fig. 2(a)) is an accumulation of 200 individual images with 5 s exposure time each, whereas for object B (Fig. 2(d)), we accumulate 300 individual diffraction images of 18 s exposure time. However, as shown below (Fig. 6), even a single acquisition of few seconds integration time is sufficient to obtain a successful reconstruction.

The recorded diffraction patterns were post-processed in several steps: First, dark counts and the background noise were removed by constant offset subtraction, and the image was centered. Second, the diffraction data was mapped onto a regularly-spaced discrete Fourier domain to account for the use of a flat detector at high numerical apertures (Ewald sphere correction) [36]. Using noise resistance modifications [37, 38], we perform reconstructions with the Hybrid Input-Output (HIO) algorithm or the Relaxed Averaged Alternating Reflections (RAAR) algorithm, starting with a random first guess and a real-space support based on the samples autocorrelation derived from the diffraction pattern. To find successful reconstructions within a maximum of 1500 iterations, the real space error in every step is compared to the errors of the two preceding ones. If a local minimum is found, the corresponding reconstruction replaces another one in an archive of 10 reconstructions, given that its error is smaller than the highest error in the archive. By the end of the run, the archive will contain 10 individual reconstructions corresponding to the 10 minima with the lowest errors among all iterations, which can be averaged in a high-quality reconstruction. In this process, the RAAR algorithm displayed somewhat faster convergence. For this extended (autocorrelation-based) support, employing a positivity constraint in real space (limiting phase variations to less than π) was required to consistently obtain successful reconstructions. However, avoiding the positivity constraint is desirable and physically warranted, and this is achieved with an improved support definition
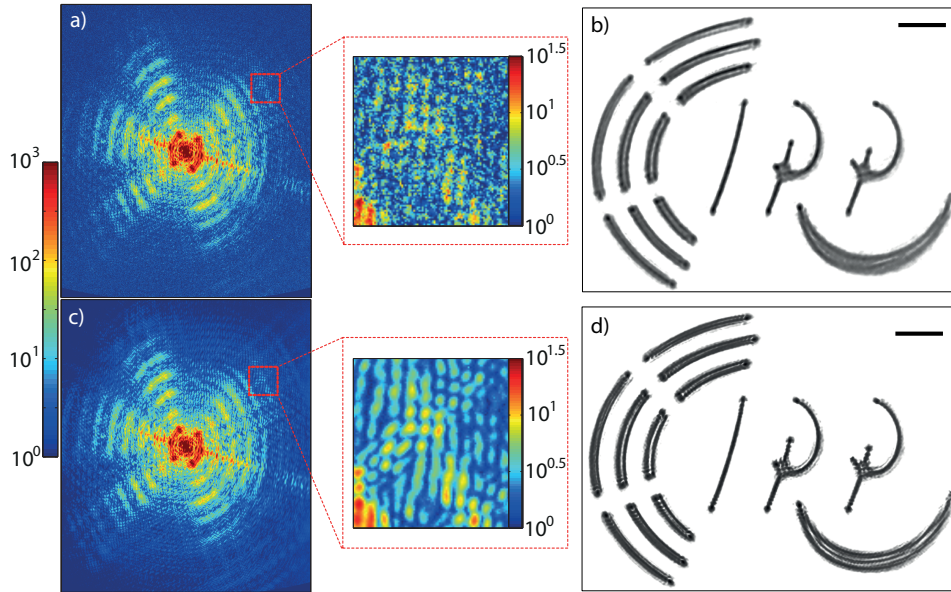
Fig. 6. (a) Single acquisition (5 s exposure time) diffraction data; logarithmic color scale. (b) Reconstructed amplitude based on diffraction pattern in (a). (c) Average of 200 individual acquisitions and corresponding reconstruction (d). Scale bars: 1 μm.

obtained by thresholding the reconstructed amplitudes after a first complete reconstruction. In addition, use of a tighter support accelerates conversion. Reconstructed amplitudes are shown in Fig. 2(b), 2(e) and Fig. 6(d), and phases are shown in Fig. 2(c), 2(f) for objects A (improved support) and B (autocorrelation support), respectively. Alternatively, the autocorrelation support can be continuously redefined during the first reconstruction run by repeatedly applying a threshold to the current reconstruction after a given number of steps, resulting in a progressive shrinking of the autocorrelation support [39].

Accumulating multiple diffraction patterns improves the signal-to-noise ratio at high diffraction angles and therefore enhances the quality of the reconstruction. Nonetheless, the majority of the objects information is already contained in a single acquisition of few seconds integration time. Figure 6 compares the reconstruction using an individual acquisition (single exposure of 5 s, corresponding to 5000 laser pulses) and that from averaging 200 individual acquisitions. The latter exhibits improved resolution and detail in the waveguide-induced amplitude modulations.

The resolution limit in the reconstructions is connected to the reliability, with which phases at high spatial frequencies are retrieved, and can be estimated using the so-called phase retrieval transfer function (PRTF) [10, 28]. In our case, the PRTF evaluates the momentum-dependent consistency of retrieved phases within 30 independent reconstructions, ranging from 1 (full convergence) to 0 (no reliable phase retrieval). Figure 7 shows the PRTF plot of the reconstruction of object A. The PRTF values are above 0.5 for all detected spatial frequencies up to 16 μm^{-1}, corresponding to a half-period resolution of about 31 nm, limited only by the diffraction.

To estimate the resolution we performed 10 individual reconstructions using the RAAR algorithm for 500 iterations with constant relaxation parameter β of 0.9999 and autocorrelation support. The reconstruction with the smallest error was chosen to define a new real space support by thresholding to 20% of the absolute value of the reconstruction. Staring from a random
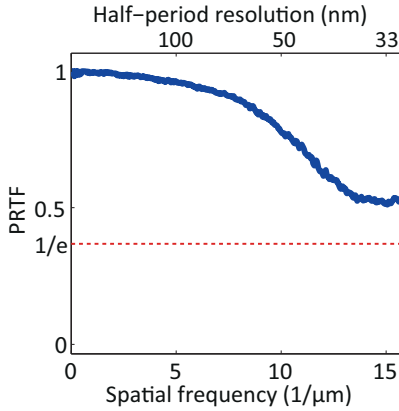
Fig. 7. Phase retrieval transfer function for the reconstructions shown in Fig. 2(b) and 2(c).

first guess but using the updated real space support another 30 reconstructions were executed with 500 iterations of RAAR. Utilization of redefined support guarantees no flipping of the reconstruction within the support and improves the convergence speed. After first 400 steps in every run, 10 local minima with the lowest errors were averaged and β parameter was decreased by 0.2 from 0.999 after every consequent 25th iteration giving the final reconstruction that was used in the PRTF computation.

Appendix D: waveguide simulations

Various theoretical approaches were taken to compute the wave propagation within the structures, including finite element (Fig. 3) and finite difference modeling [32]. We approximated the slit-type aperture regions as two-dimensional slab geometries and found this to be a good approximation. The propagation constants and transmission coefficients shown in Fig. 4 were computed using a modal expansion for slab waveguides with a cladding of complex refractive index as described in Ref. [35]. The underlying characteristic equations for transverse electric (1) and transverse magnetic (2) modes are:

$$k_w h = 2 \arctan^{-1} \frac{\gamma}{k_w} + m\pi \tag{1}$$

$$k_w h = 2 \tan^{-1} \frac{n_w^2 \gamma}{n_c^2 k_w} + m\pi \tag{2}$$

Here, h is the waveguide width, m is the mode number, $k_w = (n_w^2 k_0^2 - \beta^2)^{1/2}$ and $\gamma = (\beta^2 - n_c^2 k_0^2)^{1/2}$ represent the transverse wavenumbers in the slab and cladding, where n_c and n_w are the complex refractive indices of the cladding and waveguide materials (vacuum in our case); $k_0 = w/c$ is the vacuum wavenumber and β is the propagation constant.

Appendix E: examining Fourier truncations

In order rule out possible artifacts from Fourier truncation on the spatial amplitude fluctuations in the reconstructions, we simulated the influence of the finite-sized detector. Figure 8(a) shows a bitmap image of the object as employed in the focused ion beam fabrication, together with a close-up and a lineout with the ideal binary contrast. In Fig. 8(b), the magnitude of the Fourier
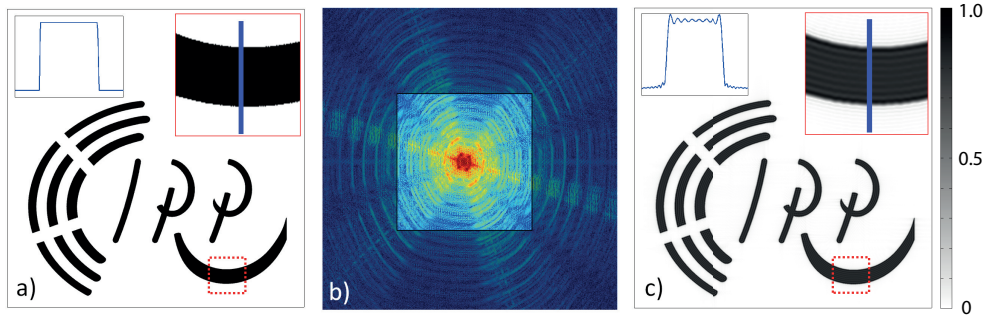
Fig. 8. (a) Bitmap image of the apertures in object A. Insets show a close-up (dashed red box) and a lineout (blue solid). (b) Magnitude of two-dimensional Fourier transform of the binary object. The inner part corresponds to the range of scattering angles collected by the detector area. (c) Inverse Fourier transform after truncation to the detector area. Minor fluctuations at high spatial frequencies are found. The features are clearly distinct from the waveguiding observed in the experiments (e.g., Fig. 3).

transform of the object is displayed on a logarithmic scale, and the inner non-shaded part corresponds to the range of Fourier components collected by the detector area (Ewald sphere curvature ignored here for simplicity). Figure 8(c) shows the resulting modulations induced by this truncation in the inverse Fourier transformation. The rather weak modulation depth and high uniform spatial frequency are very different from the waveguiding features we have identified in the experiments (Fig. 3). Therefore, it is clear that truncation artifacts do not contribute in a noticeable manner to the observations.

Acknowledgments